TEL AVIV UNIVERSITY

The Iby and Aladar Fleischman Faculty of Engineering

The Zandman-Slaner School of Graduate Studies

UTILIZING FLUORESCENT SINGLE-WALLED CARBON NANOTUBE FOR MONITORING THE FORMATION OF FIBRIN CLOTS AS PART OF THE COAGULATION CASCADE

A thesis submitted toward the degree of

Master of Science in Biomedical Engineering

by

Efrat Gerstman

May 2023

TEL AVIV UNIVERSITY

The Iby and Aladar Fleischman Faculty of Engineering

The Zandman-Slaner School of Graduate Studies

UTILIZING FLUORESCENT SINGLE-WALLED CARBON NANOTUBE FOR MONITORING THE FORMATION OF FIBRIN CLOTS AS PART OF THE COAGULATION CASCADE

A thesis submitted toward the degree of

Master of Science in Biomedical Engineering

by

Efrat Gerstman

This research was carried out in The Department of Biomedical Engineering

Under the supervision of Dr. Gili Bisker

May 2023

Acknowledgment

I would like to acknowledge my supervisor, Dr. Gili Bisker, for her continuous guidance and support professionally, and patience throughout the process.

I would like to thank Dr. Adi Hendler-Neumark, Dr. Verena Wulf and everyone in the Bisker Lab group for helpful discussions that made a substantial impact on this work.

Lastly, to Eliezer and my family, for continually believing in me, supporting me, and pushing me to succeed.

Abstract

Blood coagulation is a critical defense mechanism against bleeding that results in the conversion of liquid blood into a solid clot through a complicated cascade, which involves multiple clotting factors. One of the final steps in the coagulation pathway is the conversion of fibrinogen to insoluble fibrin mediated by thrombin. Since coagulation disorders can be life-threatening, the development of novel methods for motoring the coagulation cascade dynamics is of high importance.

Here, we use near-infrared (NIR) fluorescent single-walled carbon nanotubes (SWCNTs) to image and monitor fibrin clotting, in real-time. SWCNTs can be described as graphene sheets rolled up into long, hollow cylinders that fluoresce in the near-infrared (NIR) spectral region. SWCNTs become favorable as fluorescent sensors for biomedical applications. Following the binding of fibrinogen to a tailored SWCNT platform, thrombin transforms the fibrinogen into fibrin monomers, which start to polymerize. The SWCNTs are incorporated within the clot and can be clearly visualized in the NIR fluorescence channel, where the signal-to-noise ratio is improved compared to bright-field imaging in the visible range. Moreover, the diffusion of individual SWCNTs within the fibrin clot gradually slows down after the addition of thrombin, manifesting a coagulation rate that depends on both fibrinogen and thrombin concentrations. Our platform can open new opportunities for coagulation disorders diagnostics and allow for real-time monitoring of the coagulation cascade with NIR optical signal output in the biological transparency window.

Publications

“Monitoring the formation of fibrin clots as part of the coagulation cascade using fluorescent single-walled carbon nanotubes”

Efrat Gerstman, Adi Hendler-Neumark, Verena Wulf, and Gili Bisker

ACS Applied Materials & Interfaces, 2023, 15, 21866.

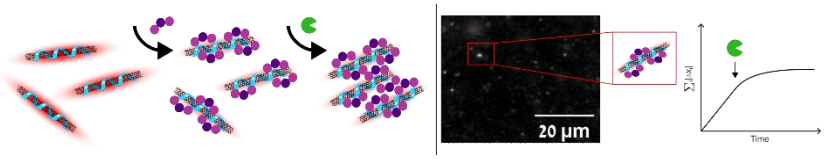

Dysfunctions in the coagulation process can lead to bleeding disorders or an increased risk of blood clots. Gerstman et. al. offer a platform for monitoring the formation of fibrin clots and for visualizing, localizing, and tracking the clots in the near-infrared (NIR) range with both spatial and temporal resolution, using NIR-fluorescent single-walled carbon nanotubes (SWCNTs).

Table of contents

List of Figures

1. Introduction

1.1 Blood coagulation

1.1.1 Coagulation process

Blood coagulation is an important defense mechanism against bleeding. Rapture of the endothelium allows blood exposure to the extravascular tissue, which initiates the extrinsic coagulation pathway,[1,2] while the intrinsic pathway is initiated by coagulation factors (CF) in the blood.[3] Both activation pathways lead to a common pathway, which includes the conversion of fibrinogen (CF I) to fibrin (CF Ia), by thrombin (CF IIa) (Figure 1).[4]

Fibrinogen, a soluble plasma glycoprotein secreted by the liver, is the most abundant protein in the plasma with normal physiological concentrations of 1.75-4.3 g L^{-1},[5] and the main building block of blood clots. It also acts as an adhesive protein essential for platelet aggregation. Fibrinogen has an elongated structure with three domains, a central E-domain, and two terminal D-domains.[6] The conversion of fibrinogen to insoluble fibrin involves the proteolytic release of two fibrinopeptides from the amino-terminal ends of the polypeptide chains, and it is catalyzed by the enzyme thrombin. The resulting fibrin monomers spontaneously polymerize forming a fibrin clot.[7,8]

Thrombin plays a key role in the coagulation cascade as it is responsible for activating fibrinogen and regulating its aggregation. A cascade of coagulation factors initialize the cleavage of prothrombin to thrombin, which then catalyzes the cleavage of fibrinogen, and amplifies the coagulation through a positive feedback loop.[1,9–12]

Thrombin has two surface regions termed exosite I and exosite II. Exosite I is the fibrinogen-binding domain, and it is required for the recognition of additional substrates.

Exosite II is a heparin-binding domain, and it is essential for the inhibition of thrombin by antithrombin.[9,13–16]

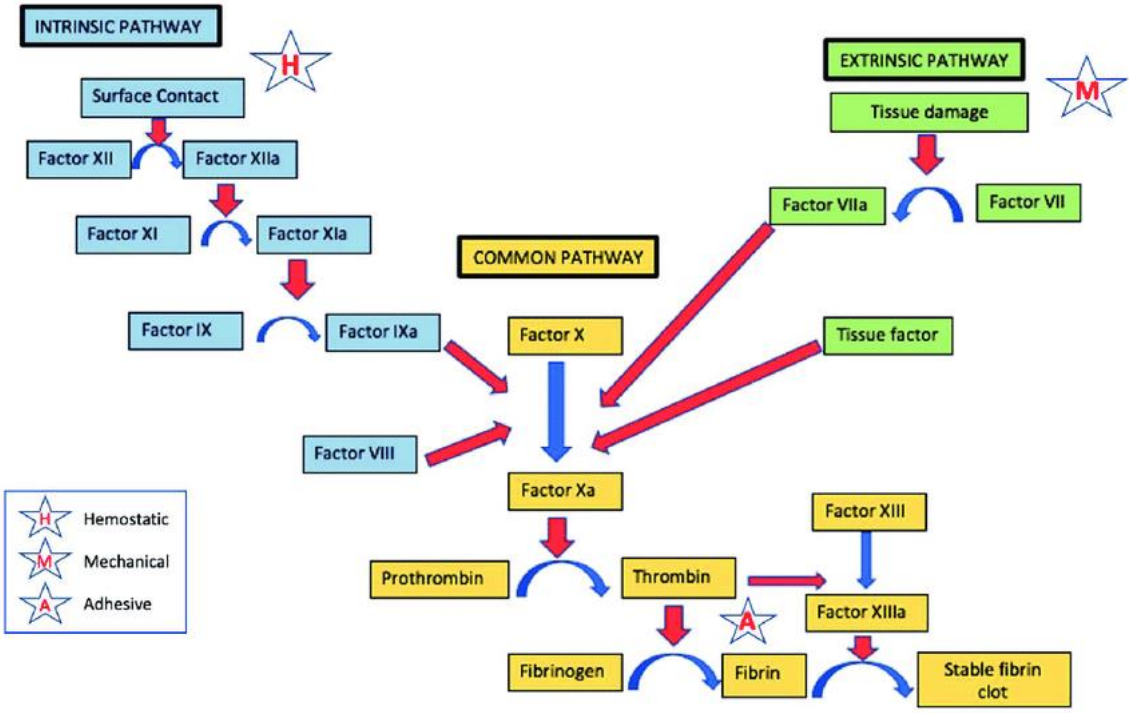

Figure 1. Diagram of coagulation cascade including intrinsic (blue) and extrinsic pathway (green). Both pathways combine into the common pathway (yellow) leading to activation of factor X and then subsequent thrombin-fibrin activation and finally formation of the fibrin clot.[17]

1.1.2 Coagulation tests

The coagulation system is essential for maintaining the balance of blood fluidity and hemostasis. The absence or reduced production of thrombin can result in hemorrhagic diseases like hemophilia,[18–21] whereas unregulated thrombin production can result in thrombotic occlusion.[22–24] Moreover, individuals with congenital fibrinogen deficiency can suffer from uncontrolled bleeding,[6] whereas elevated levels of fibrinogen increase the risk of thrombosis[25] and may compromise clot stability.[26]

Prothrombin time (PT) and activated partial thromboplastin time (APTT) are the most common coagulation tests. The PT test involves the determination of the time for a clot formation in a plasma sample after initiating the extrinsic coagulation pathway by the

addition of tissue factor (TF) and calcium.[27–31] The APTT test, on the other hand, measures the clotting time of the intrinsic pathway, which is initiated by the addition of calcium and APTT reagents, containing partial thromboplastin and an intrinsic pathway activator.[32,33] Since both tests measure the clotting time, they give information only about the endpoint of the coagulation cascade, where abnormal results require further testing to find the source of the problem.

Two alternative coagulation tests are rotational thromboelastography (ROTEM) and thromboelastography (TEG). These tests are performed on whole blood and measure the viscoelasticity of the blood sample during clot formation in real-time. By applying an external shear to mimic blood flow conditions, the kinetics and strength of the sample are monitored during the clotting process.[34] While both ROTEM and TEG measure the viscoelastic properties of the blood sample in real-time, they only provide bulk properties, without microscopic or spatial information.

Many approaches have been developed to detect fibrinogen or thrombin, such as surface plasmon resonance (SPR),[35–38] quartz crystal microbalance (QCM),[39] fluorescence,[40–42] magnetic,[43] colorimetric[44,45] and electrochemical analyses.[46–48] These approaches provide information on the fibrinogen or thrombin concentration but do not provide dynamic information on the coagulation process or the coagulation rate. Other technologies for point-of-care measurements rely on optical, electro-mechanical, photoacoustic, electrical impedance spectroscopy, and magnetoelasticity for assessing the clotting time, however, their main application is PT and APTT tests.[49,50] Therefore, new methods for assessing the coagulation process that can provide dynamic information throughout the cascade would benefit blood coagulation research and advance new diagnostic tools.[51]

1.2 Single-walled carbon nanotubes

1.2.1 Structure and properties

Single-walled carbon nanotubes (SWCNTs) can be described as graphene sheets rolled up into long, hollow cylinders of 0.7-3 nm in diameter, and length of 300 nm – 10 μm (Figure a), where different rolling orientations of the graphene sheets lead to different chiralities of the nanotubes.[52] Because the SWCNTs properties can change depending on their structure, each chirality has a different diameter and physical, chemical, electronic, and optical properties.[53–55]

The angle values can be described using two integer values - a_1 and a_2, which denotes the lattice basic vectors of the graphene layer (Figure b). The roll up angle of the SWCNT can be described by a vector that is a linear combination of the two:

$$c = na_1 + ma_2 \quad (1)$$

The different geometries are described by the (n,m) index and are known as the SWCNTs chirality. The (n,m) index is related to diameter of the SWCNT:

$$d = \frac{|c|}{\pi} = \frac{a_0}{\pi}\sqrt{n^2 + nm + m^2} \quad (2)$$

Where a_0 is the graphene lattice constant (0.246 nm).

The (n,m) values also describe whether SWCNTs exhibit metallic, semimetallic, or semiconducting properties. The density of electronic states, as well as the band gap between the conduction and valence bands are related to these properties and determine whether a SWCNT is fluorescent.[54] Due to the electronic band-gap between the valence and conduction bands, semiconducting SWCNTs fluoresce in the nIR.[56] Transitions from the conduction to the valence band lead to fluorescence, where the E_{22} transitions lead to absorption (v2 → c2) and the E_{11} transition to the fluorescence emission (c1 → v1) (Figure 2c).[56]

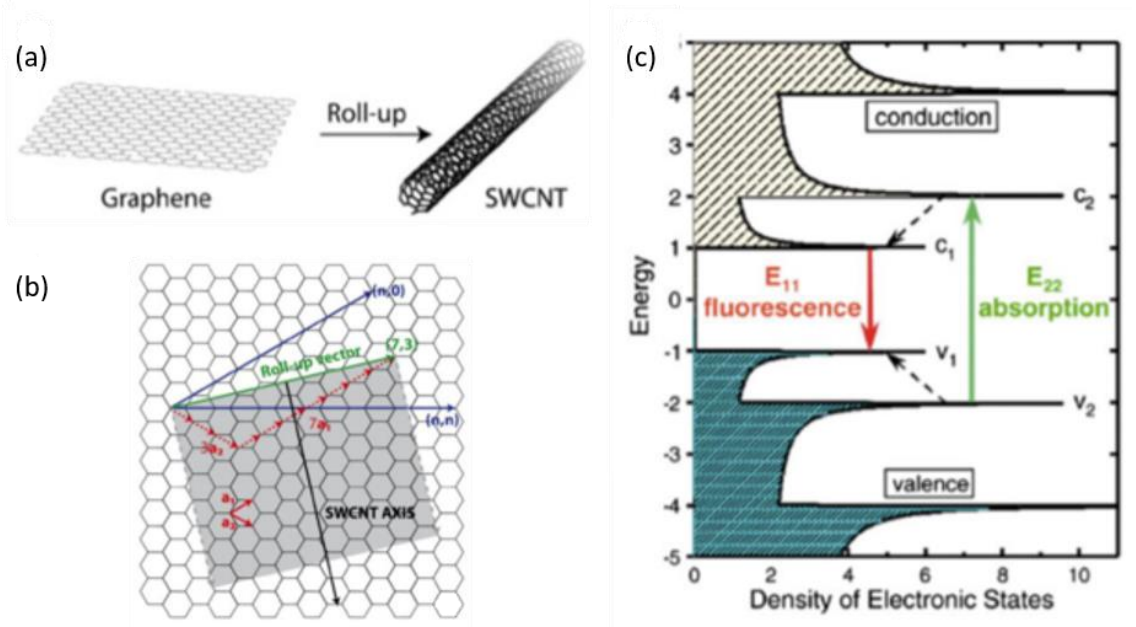

Figure 2. SWCNT's structural properties. a) Illustration of SWCNTs consist of a graphene sheet rolled up to form a cylinder. b) The roll up vector c is defined as $c = na_1 + ma_2$. SWCNT are generated by rolling up the graphene sheet along this vector and superimposing the first and the last carbon atom. An example (green) for the (7, 3) SWCNT is given where $c = 7a_1 + 3a_2$. c) Density of electronic states of a semiconducting SWCNT.

Unfunctionalized SWCNTs are hydrophobic, and due to strong van der Waals forces, form bundles.[57] The high surface area of SWCNTs allows them to be functionalized with amphiphilic molecules or polymers,[58] and to form a colloidal suspension of individually dispersed SWCNTs.[58,59]

1.2.2 SWCNTs as fluorescent biosensors

Semiconducting SWCNTs fluoresce in the near-infrared (NIR) spectral region, mainly between 900 and 1400 nm, where biological samples are primarily transparent.[56,60–62] Further, SWCNT do not photobleach or blink upon use, provide spatiotemporal information, are stable at room temperature, and are biocompatible long-term *in vivo*.[63,64,73,74,65–72] Due to these unique optical properties, SWCNTs become favorable as fluorescent sensors for biomedical applications.[58,59,83–88,75–82] The mechanism of

SWCNT-based sensors relies on a heteropolymer that is adsorbed onto the SWCNTs surface and mediates the binding of a specific target analyte. Analyte binding then modifies the spectral properties of the NIR fluorescence emission of the SWCNTs providing optical signal readout in real-time.[89–94] This approach has been demonstrated to recognize numerous analytes ranging from small molecules[95–102] to large proteins and enzymes.[103–111]

1.2.3 SWCNT fibrinogen sensor

Following a high throughput screening assay, SWCNTs functionalized by dipalmitoyl-phosphatidylethanolamine (DPPE)-polyethylene glycol (PEG) were discovered as a fibrinogen sensor.[5] The DPPE-PEG-SWCNT sensor showed a decrease in the SWCNT fluorescence intensity depending on the fibrinogen concentration and could be used to detect and quantify fibrinogen. The fibrinogen was shown to physically bind the SWCNT surface and align along the principal axis of the nanotube, where atomic force microscopy (AFM) imaging revealed the complete binding of the three globular domains of fibrinogen to the SWCNT surface. Moreover, the binding could not be correlated to any nonselective parameters such as the molecular weight, hydrophobicity, or iso-electric point, and was thus attributed to structural recognition by the SWCNT corona phase.[5]

2. Research goal

In this work, we aim to show that the DPPE-PEG-SWCNT fibrinogen sensor can be used as a platform to monitor the catalytic activity of thrombin and visualize the fibrin clot formation, thus providing real-time dynamic information about the coagulation process. We rely on the binding of fibrinogen to DPPE-PEG-SWCNT and the conversion of fibrinogen to fibrin in the presence of thrombin (Figure 3a). The introduction of thrombin to DPPE-PEG-SWCNT – fibrinogen, initiates the polymerization of the fibrin monomers, resulting in fibrin clots that encapsulate the SWCNTs (Figure 3b).[5] While the binding of fibrinogen to the SWCNT results in a decrease in the fluorescence intensity, the addition of thrombin does not affect the SWCNT fluorescence emission (Figure 3b). Nevertheless, the SWCNTs are incorporated within the fibrin clots, and can be visualized via 2D NIR-fluorescence imaging (Figure 3c) to provide spatiotemporal information on the clotting process. Moreover, single-SWCNT tracking reveals a gradual slowing down of the SWCNT diffusion during the fibrin polymerization process, with both fibrinogen and thrombin concentration-dependent rates. Our platform provides direct visualization of fibrin clotting in real-time with a spatiotemporal resolution, and can advance the current research and diagnostic tools for the coagulation cascade.

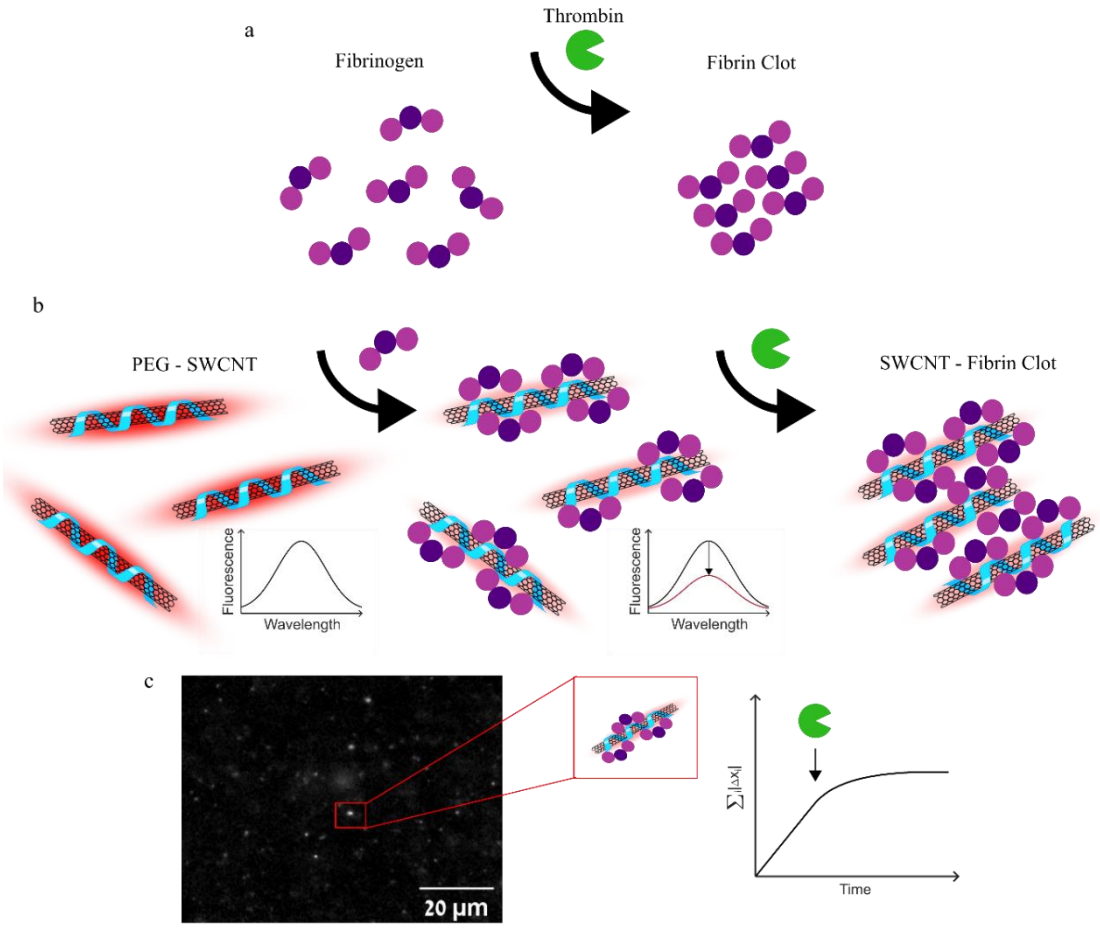

Figure 3. Schematic illustration of the work's protocol. a) Schematic illustration of the fibrin coagulation process. Thrombin catalyzes the conversion of fibrinogen to fibrin, which polymerizes to form a clot. b) Fibrinogen binds to DPPE-PEG-SWCNT, resulting in a decrease in fluorescence intensity. The addition of thrombin leads to clot formation incorporating the DPPE-PEG-SWCNTs. c) Tracking individual NIR-fluorescent DPPE-PEG-SWCNTs during clot formation shows a gradual slowing down of the SWCNT diffusion following the addition of thrombin.

3. Methods

3.1 SWCNT suspension

SWCNTs (HiPCO, NanoIntegris) were first suspended with 2 wt% sodium-cholate (SC, Sigma Aldrich) *via* bath sonication (Elma P-30H, 80 Hz for 10 min, room temperature), followed by direct tip sonication (QSonica Q125, 12 W for 30 min twice) in an ice bath. To remove SWCNT aggregates and impurities, the suspension was ultracentrifuged (OPTIMA XPN-80, 41,300 rpm for 4 h), and the top 80% of the supernatant was collected. Subsequently, a surfactant exchange was performed. To this means, a mixture of SC-suspended SWCNTs (40 mg L^{-1}) and 2 mg mL^{-1} DPPE-PEG(5000kDa) was dialyzed against water using a dialysis cartridge (Repligen, MWCO: 1 kDa). Dialysis was performed for 5 days at room temperature with multiple water exchanges to remove sodium cholate and allow the adsorption of the DPPE-PEG onto the SWCNTs.

3.2 Absorption spectroscopy

A successful suspension was validated by observing distinguishable peaks in the absorption spectra of the suspensions using a UV-vis-NIR spectrophotometer (Shimadzu UV-3600 PLUS), where redshift relative to SC-SWCNT suspension indicated SC surfactant exchange.

The absorption spectra of a SWCNTs solution with fibrinogen and thrombin were recorded using a UV-vis-NIR spectrophotometer (Shimadzu UV-3600 PLUS). Briefly, 400 µl of 5 mg L^{-1} DPPE-PEG-SWCNTs were measured with 0 or 2.5 mg mL^{-1} fibrinogen, and 0 or 0.01 mg mL^{-1} thrombin in PBS. The absorption was recorded between 400-1300 nm (1 nm step size).

3.3 Near-IR fluorescence spectroscopy

Fluorescence emission spectra were recorded in a 96-well-plate mounted on an inverted microscope (Olympus IX73). A super-continuum white-light laser (NKT-photonics, Super-K Extreme) with a bandwidth filter (NKT-photonics, Super-K Varia, $\Delta\lambda$ = 20 nm) was coupled into the microscope as the excitation source. Fluorescence emission was spectrally resolved using a spectrograph (Spectra Pro HRS-300, Teledyne Princeton Instruments) with a slit-width of 500 µm and a grating (150 g mm^{-1}). The fluorescence intensity spectrum was recorded by an InGaAs-detector (PyloNIR, Teledyne Princeton Instruments).

For validation of successful suspension, the fluorescence spectra of 100 µl of 1 mg L^{-1} SC-SWCNT or DPPE-PEG-SWCNT suspension were recorded at an excitation wavelength of 730 nm (20 mW) with an exposure time of 1 s. Redshift in the DPPE-PEG-SWCNT fluorescence spectrum relative to SC-SWCNT suspension indicated SC surfactant exchange.

For the fluorescence spectra of DPPE-PEG-SWCNT with fibrinogen and thrombin, 100 µl of 1 mg L^{-1} SWCNT suspension were incubated with fibrinogen for 1 h. Then, thrombin was added and incubated for 20 min. The fluorescence spectra were recorded at an excitation wavelength of 730 nm (20 mW) with an exposure time of 1 s.

To quantify the DPPE-PEG-SWCNT-fibrinogen interaction, the fluorescence peak intensity of the (9,4)-chirality was determined, and its concentration-dependent response on the addition of fibrinogen was fitted with a two-step sequential binding model of the DPPE-PEG-SWCNT-fibrinogen interaction, the data were fitted by the equation:[5]

$$\frac{I-I_0}{I_0} = \beta\left(1 - \frac{1}{1+K_{d1}^{-1}[L]+(K_{d1}K_{d23})^{-1}[L]^3}\right) \quad (3)$$

where I_0 is the initial fluorescence intensity, I is the final fluorescence intensity, L is the fibrinogen concentration, β is a proportionality factor, and K_{d1} and K_{d23} are the dissociation constants. The resulting fit parameters were β = -0.59, K_{d1} = 0.0115 mg mL^{-1} and K_{d23} = 2.21 x 10^{-5} mg^2 mL^{-2}.

Excitation-emission maps were recorded on samples of 1 mg L^{-1} DPPE-PEG-SWCNTs in PBS with 0.5 mg mL^{-1} fibrinogen or without fibrinogen using an excitation wavelength range of 500 nm to 840 nm in 2 nm steps with an exposure time of 1 s.

3.4 Transmission Electron Microscopy (TEM)

30 µl of the sample solutions: 5 mg L^{-1} DPPE-PEG-SWCNT, 5 mg L^{-1} DPPE-PEG-SWCNT with 5 mg mL^{-1} fibrinogen, fibrin clot from 5 mg mL^{-1} fibrinogen and 5 µg mL^{-1} thrombin, and similar concentration of fibrin clot with 5 mg L^{-1} DPPE-PEG-SWCNT (in PBS, final concentration) were applied to a carbon-coated grid and stained with 10 µl of 2% (w/v) uranyl acetate solution. After blotting with excess stain solution, the grid was left to air dry. The negatively stained samples were imaged using a JEM-1400Plus TEM (Jeol, Japan). Images were captured using SIS Megaview III camera, iTEM the TEM imaging platform (Olympus).

3.5 Scanning Electron Microscopy (SEM)

40 µl of the sample solutions: fibrin clot from 5 mg mL^{-1} fibrinogen and 5 µg mL^{-1} thrombin and similar concentration of fibrin clot with 5 mg L^{-1} DPPE-PEG-SWCNT (in PBS, final concentration) were dried under vacuum and coated with 5 nm gold particles. The samples were imaged using a HRSEM (Zeiss GeminiSEM 300) with an EDS detector (X-Flash 6/60, Bruker).

3.6 2D Fluorescence imaging

Fluorescence images were taken via an inverted fluorescence microscope (Olympus IX83) through a 100X TIRF objective (Olympus UAPON 100XOTIRF). The SWCNT-fluorescence was excited by a 730 nm CW laser (MDL-MD-730-1.5W, Changchun New Industries). The laser excitation light was directed to the samples with a dichroic mirror (900 nm long-pass, Chroma), and the NIR emission of the SWCNTs was detected after an additional 900 nm long-pass emission filter (Chroma, ET900lp) with an InGaAs camera (Raptor, Ninox 640 VIS-NIR). All images were processed by ImageJ and MATLAB.

For the SWCNT-fibrin clot images, 1 mg L^{-1} DPPE-PEG-SWCNTs, 2 mg mL^{-1} fibrinogen, and 0.002 mg mL^{-1} thrombin in PBS or in 10% Fetal bovine serum (FBS) were mixed, and the SWCNT-fibrin clot was transferred from the solution to a microscope slide.

3.7 Measurements of DPPE-PEG-SWCNTs during fibrin-clot formation

For images of the coagulation process measured in flow, a mixture of 4 mg L^{-1} DPPE-PEG-SWCNT and 2 mg mL^{-1} fibrinogen was inserted into a channel slide (Ibidi). The fluorescence images were taken at time intervals of 200 ms with an exposure time of 50 ms. After 13 s, while the images were still taken, 20 µl of 0.1 mg mL^{-1} thrombin was added into the inlet of the channel. After the formation of the clots, both brightfield and NIR images were taken.

For images of the coagulation process measured on the slide, a mixture of 20 µl of 1 mg L^{-1} DPPE-PEG-SWCNT in PBS or in 10% FBS and 2, 0.2, or 0.02 mg mL^{-1} fibrinogen was dropped on a microscope slide. The fluorescence images were taken at time intervals of 200 ms with an exposure time of 150 ms. After a few seconds, while the images were still taken, 10 µl of thrombin was added to obtain final concentrations of 13, 1.3, or 0.13 µg mL^{-1} to the SWCNT-fibrinogen solution on the microscope slide.

SWCNT displacement was calculated using the TrackMate toolbox in ImageJ.[112] To calculate the cumulative increments, the mean displacement of the particles between two consecutive frames of the movie was calculated. The cumulative increments in each time are the sum of the mean displacement until the corresponding frame.

4. Results and Discussion

4.1 DPPE-PEG-SWCNT suspension and functionalization with fibrinogen

In order to functionalize SWCNTs with fibrinogen, we used DPPE-PEG suspended SWCNTs, which were previously shown to bind fibrinogen specifically, even in a serum environment.[5] SWCNTs were first suspended by sodium cholate (SC), which was then exchanged to DPPE-PEG via dialysis, as evident from the redshift of the absorption peaks (Figure 4a) and the fluorescence peaks (Figure 4b). The DPPE-PEG-SWCNTs showed bright fluorescent peaks of the various chiralities in the mixture (Figure 4c). Following the absorption of fibrinogen onto the DPPE-PEG-SWCNTs, an overall decrease in the fluorescence intensity of all the chiralities was observed (Figure 4d). The DPPE-PEG-SWCNTs concentration-dependent fluorescence intensity response to fibrinogen (Figure 4e) could be calibrated to the fibrinogen concentration, reaching the maximal saturated value at approximately 0.012 mg mL^{-1} (Figure 4f). The ability of fibrinogen to be efficiently adsorbed onto the DPPE-PEG-SWCNTs demonstrates that the SWCNTs are a promising platform to be integrated into the fibrin clots, even at low fibrinogen concentrations, and provide optical signal readout in the NIR range for visualization, localization, and tracking.

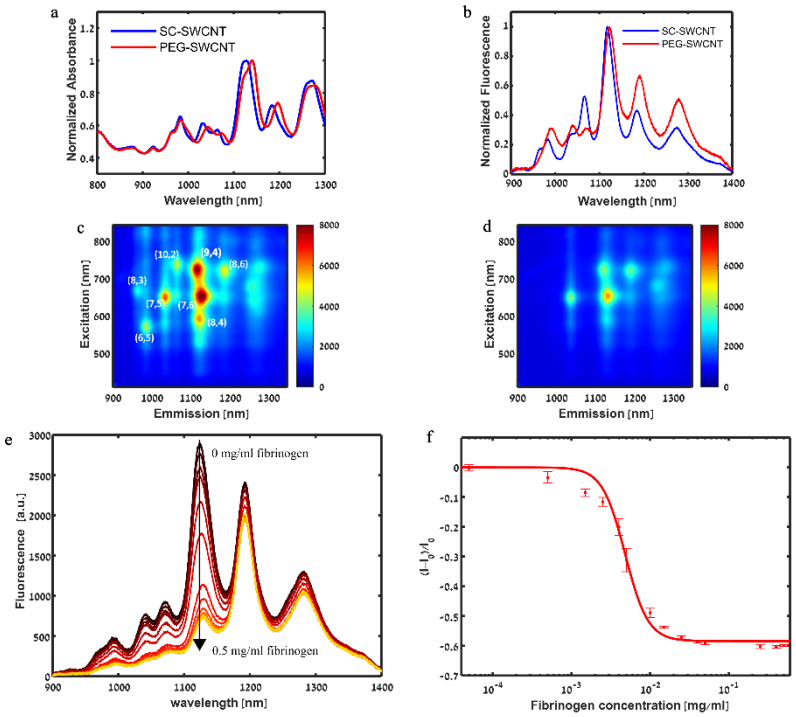

Figure 4. DPPE-PEG-SWCNTs as a platform for fibrinogen absorption. a) Absorption spectra of SC-SWCNT suspension (blue) and the red-shifted DPPE-PEG-SWCNT suspension (red). b) Normalized fluorescence spectra of SC-SWCNT suspension (blue) and the red-shifted DPPE-PEG-SWCNT suspension (red). c) Excitation-emission map of the DPPE-PEG-SWCNTs, showing the various nanotube chiralities. d) Excitation-emission map of the DPPE-PEG-SWCNT solution after the addition of 0.5 mg mL^{-1} fibrinogen. e) Fluorescence emission spectra of DPPE-PEG-SWCNT under 730 nm laser excitation after incubation with 0, $5x10^{-5}$, $5x10^{-4}$, $1.5x10^{-3}$, $2.5x10^{-3}$, $4x10^{-3}$, $5x10^{-3}$, $1x10^{-2}$, $1.5x10^{-2}$, $2.5x10^{-2}$, $4x10^{-2}$, $5x10^{-2}$, 0.25, 0.4, and 0.5 mg mL^{-1} fibrinogen (black to yellow), showing a concentration-dependent decrease in fluorescence intensity. f) Normalized fluorescent response of the (9,4) chirality of the DPPE-PEG-SWCNTs to different concentrations of fibrinogen (dots). The solid line represents the fit according to equation (1), as detailed in the experimental section.

4.2 Fluorescence properties of DPPE-PEG-SWCNTs – fibrinogen in the presence of thrombin

We tested the effect of the addition of thrombin to the fluorescence intensity of the DPPE-PEG-SWCNTs in the presence and absence of fibrinogen. In contrast to fibrinogen, which led to a 42% fluorescence intensity decrease of the (9,4) chirality at a concentration of 0.5 mg mL^{-1} fibrinogen, the addition of thrombin did not affect the fluorescence emission of the DPPE-PEG-SWCNTs (Figure 5a). Similarly, the addition of thrombin following

the addition of fibrinogen had no additional effect on the SWCNTs fluorescence intensity (Figure 5a). These results suggest that fibrinogen remains bound to the SWCNT-surface even after the addition of thrombin, and that the cleavage of the fibrinopeptides converting fibrinogen to fibrin and its polymerization does not result in a modulation of the SWCNTs fluorescence. The two-step sequential binding model of fibrinogen to DPPE-PEG-SWCNT assumed a complete binding of the three globular domains of fibrinogen to the SWCNT surface, evident from atomic force microscopy (AFM) imaging.[5] The cleavage of two pairs of fibrinopeptides from the amino-terminal ends of the fibrinogen chains by thrombin[8] exposes the fibrin polymerization site, however, it does not seem to affect the binding affinity to the SWCNTs.

We have further tested the effect of thrombin on the DPPE-PEG-SWCNTs absorption. While the addition of fibrinogen results in a slight redshift in the absorption, in agreement with previous findings[5], thrombin had no effect on the DPPE-PEG-SWCNTs absorption (Figure 5b). The redshift of the DPPE-PEG-SWCNTs absorption in response to fibrinogen binding was still evident even after the addition of thrombin, further supporting that the fibrinogen remained bound to the SWCNT surface. Still, there was an overall increase in the absorption in the visible wavelength range. The increase in absorption was found to be correlated to the absorption of polymerized fibrin resulting from the addition of thrombin to fibrinogen without SWCNTs (Figure 5c), and was therefore attributed to the formation of fibrin clots (Figure 5b). The absorption increase was also reported in previous studies, where increased light scattering was indicative of aggregation due to the formation of clots.[113]

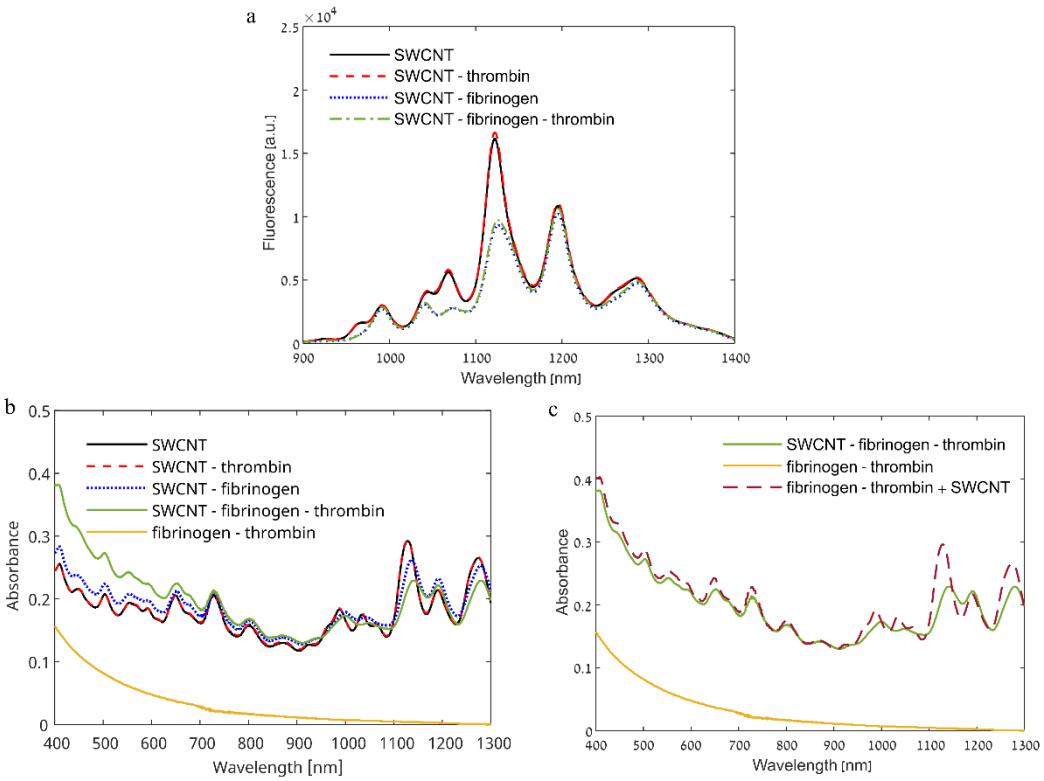

Figure 5. The effect of thrombin addition on DPPE-PED-SWCNT-fibrinogen fluorescence and absorption spectra. a) Fluorescence emission spectra of 5 mg L^{-1} DPPE-PEG-SWCNTs without proteins (black line), with 0.02 mg mL^{-1} thrombin (dashed red line), with 0.5 mg mL^{-1} fibrinogen (dotted blue line), or with both fibrinogen and thrombin (dashed-dotted green line). b) Absorption spectra of 5 mg L^{-1} DPPE-PEG-SWCNT without proteins (solid black line), with 0.01 mg mL^{-1} thrombin (dashed red line), with 2.5 mg mL^{-1} fibrinogen (dotted blue line), or with both fibrinogen and thrombin (solid green line), and the absorption of the two proteins without DPPE-PEG-SWCNT (solid yellow line). c) Absorption spectrum of 5 mg L^{-1} DPPE-PEG-SWCNT with both 2.5 mg mL^{-1} fibrinogen and 0.01 mg mL^{-1} thrombin (SWCNT – fibrinogen – thrombin, green line), absorption spectrum of the two proteins, 2.5 mg mL^{-1} fibrinogen and 0.01 mg mL^{-1} thrombin, without DPPE-PEG-SWCNT (fibrinogen – thrombin, yellow line), and the absorption spectrum of the two proteins without DPPE-PEG-SWCNT to which the absorption of DPPE-PEG-SWCNT was added (fibrinogen – thrombin + SWCNT, dashed brown line).

We have further imaged the SWCNTs using transmission electron microscopy (TEM), where we could visualize individual DPPE-PEG-SWCNT (Figure 6a) and DPPE-PEG-SWCNT-fibrinogen (Figure 6b). TEM images of the fibrin clot without (Figure 6c) and with SWCNTs (Figure 6d) showed similar fibrillary structures. Moreover, scanning electron microscope (SEM) images also showed similar fibrillary structures of the fibrin clot without (Figure 6e) and with SWCNT (figure 6f). These high-resolution imaging results confirm that the SWCNT did not affect the clot structure.

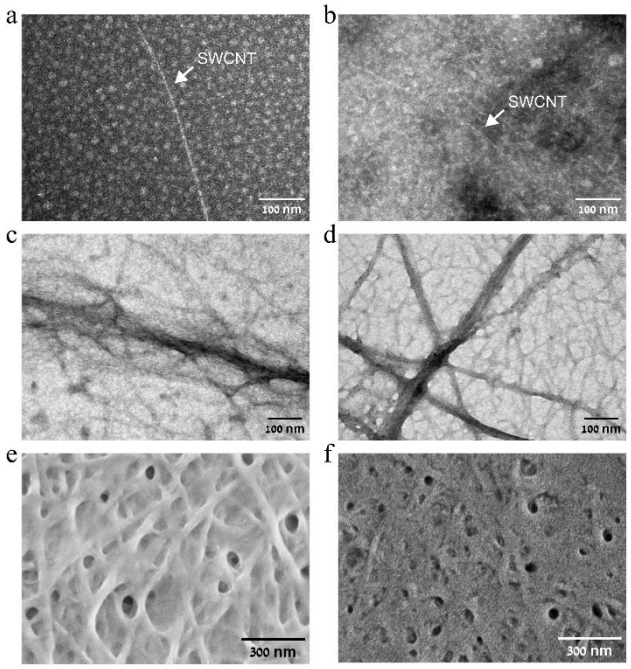

Figure 6. The effect of DPPE-PEG-SWCNT addition on the structure of the fibrin clot. a) TEM image of DPPE-PEG-SWCNT. b) TEM image of DPPE-PEG-SWCNT-fibrinogen. c) TEM image of a fibrin clot. d) TEM image of fibrin clot with SWCNT. e) SEM image of a fibrin clot. f) SEM image of fibrin clot with SWCNT. The similar fibrillary structures of the fibrin clot with or without SWCNT confirm that the SWCNT has no effect on the clot structure.

4.3 NIR-fluorescence imaging of SWCNTs incorporated into fibrin clots

Fibrin clots consist of the assembly of fibrin monomers to fibrillary structures. We assume that SWCNTs can be integrated into these fibers, due to their thin, tubular structure. The presence of SWCNTs in the fibrin clot is supported by a simple observation of the clot with SWCNTs, which shows an opaque darker color, compared to a clot without SWCNT, which is completely transparent (Figure 7a). To support the integration of the SWCNT into the fibrin fibers, we further imaged the SWCNTs-incorporating fibrin clots using bright-field and NIR-fluorescence microscopy in different magnifications (Figure 7b) and compared to bright-field images of fibrin clots without SWCNTs (Figure 8a). The fibrin

fibers are visible in the bright-field, and they show similar morphology with and without the SWCNT. Moreover, the SWCNTs clearly maintain their fluorescence emission, and we observe a co-localization between the NIR fluorescence and the fibrin fibers. This correlation between the spatial distribution of the NIR fluorescence of the SWCNTs and the spatial distribution of the fibrin fibers seen in the bright-field images affirm the integration of the SWCNT into the fibers. These results ensure that the addition of thrombin does not lead to unbinding of fibrinogen from the DPPE-PEG-SWCNT surface and that SWCNTs do not hinder clot formation. In addition, we have imaged the SWCNTs-incorporating fibrin clots in 10% Fetal bovine serum (FBS) and saw a similar co-localization between the SWCNTs and the fibrin fibers (Figure 8b), indicating that the SWCNT-fibrin integration also occurs in a more complex environment.

Since DPPE-PEG-SWCNTs can be incorporated with the fibrin clot, they can also serve as NIR-fluorescence staining for the clots in solution. To demonstrate such staining, a DPPE-PEG-SWCNT–fibrinogen solution was inserted into a channeled μ-slide, to which thrombin was added. After the formation of clots, both brightfield and NIR fluorescence images were taken (Figure 7c). While in the brightfield images, the clots can only be visualized in solution with very low contrast, the NIR fluorescence images allow us to clearly identify the clots, and characterize their size and location.

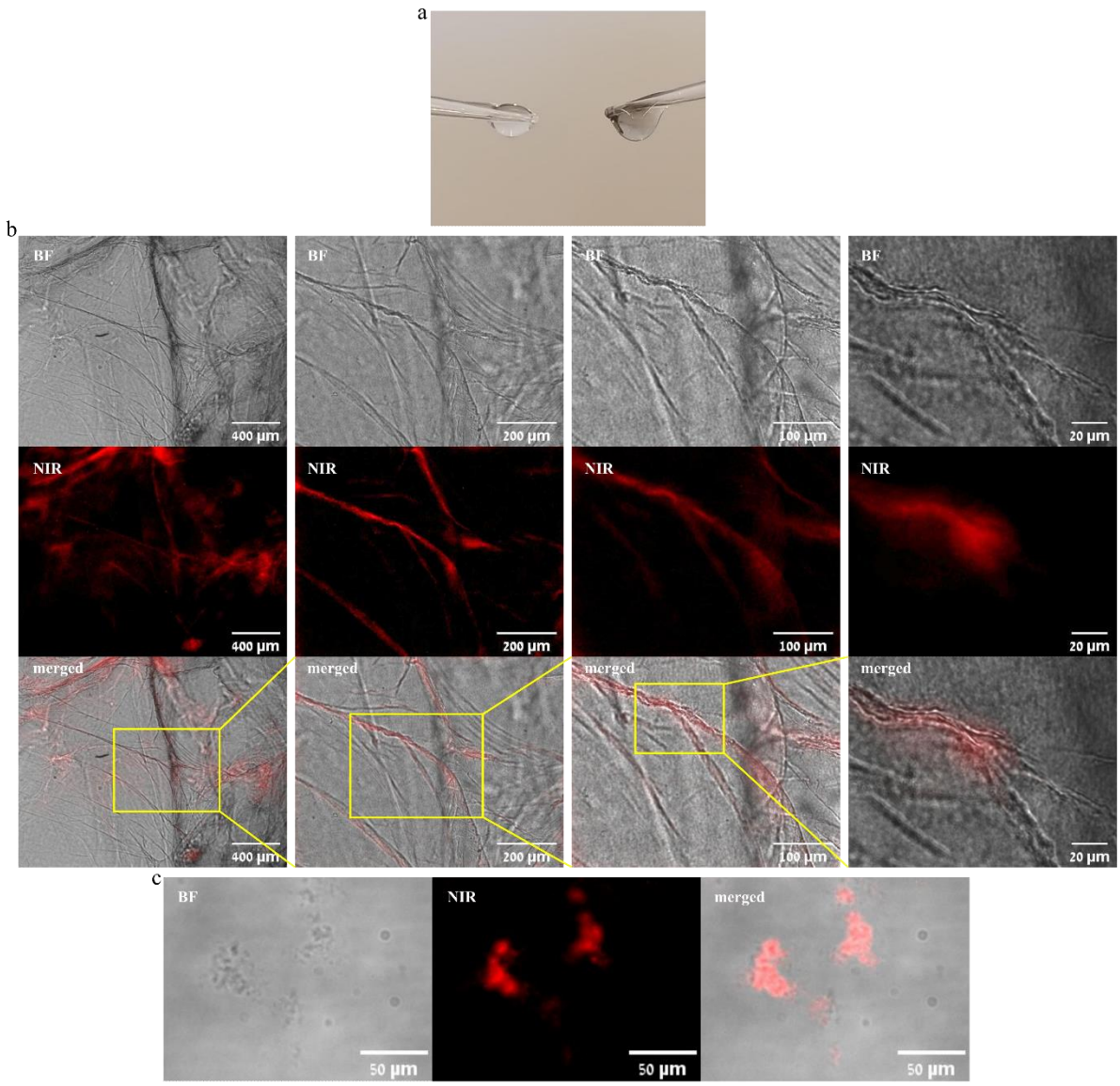

Figure 7. NIR-fluorescence imaging of DPPE-PEG-SWCNTs incorporated into fibrin clots. a) Image of a fibrin clot (left) and a fibrin clot with DPPE-PEG-SWCNT (right). b) Brightfield (BF), NIR-fluorescence (NIR), and merged images of the DPPE-PEG-SWCNT-fibrin clot. Images were taken with 4x, 10x, 20x, or 60x magnification (from left to right). Each image shows the ROI marked in the image to the left. c) Brightfield, NIR-fluorescence, and merged image of DPPE-PEG-SWCNT-fibrin clot in solution.

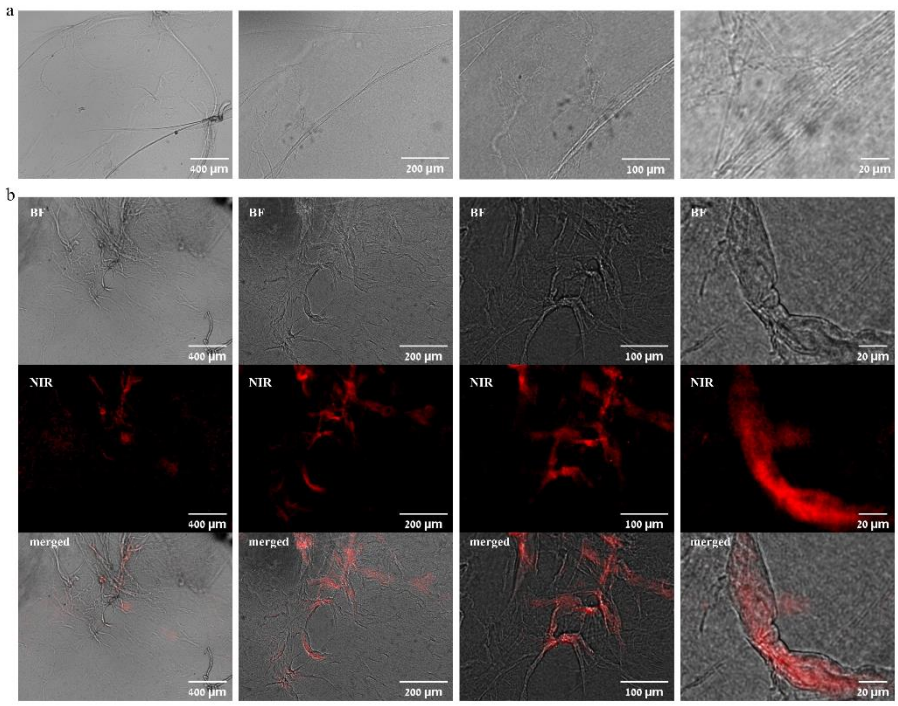

Figure 8. Imaging of fibrin clots. a) Brightfield images of fibrin clots in PBS without DPPE-PEG-SWCNTs. Images were taken with 4x, 10x, 20x, or 60x magnification (from left to right). b) NIR-fluorescence imaging of DPPE-PEG-SWCNTs incorporated into fibrin clots in 10% Fetal bovine serum (FBS). Brightfield (BF), NIR-fluorescence (NIR), and merged images of the DPPE-PEG-SWCNT-fibrin clot. Images were taken with 4x, 10x, 20x, or 60x magnification (from left to right).

4.4 Spatiotemporal monitoring of the clot formation via NIR-fluorescence imaging

After we have established that the SWCNT can serve as NIR fluorescence staining for the clot, we further aim to monitor the dynamics of the clotting process. To this end, we continuously imaged the clot formation following the addition of thrombin in two different configurations, namely, in a microfluidic device under flow, and on a microscope slide in a diffusion-driven process.

To image the clotting process in a microfluidic channel, the SWCNT-fibrinogen suspension was inserted into a μ-slide channel. The NIR-fluorescence of the SWCNT was imaged continuously while thrombin was added to the inlet of the channel. Figure 9a shows snapshots at different time points from the movie, showing that prior to thrombin addition, the SWCNTs appeared to be distributed throughout the solution as individual nanotubes without clusters. On the other hand, the addition of thrombin, and the conversion of fibrinogen to fibrin, lead to big fibrin clots of approximately 20 μm in diameter. The flow, in this case, accelerates the mixing so that small clots can bind and coalesce. These clots could be visualized, owing to the incorporated DPPE-PEG-SWCNTs, as high intensity fluorescent clusters in the image.

When thrombin was added to a droplet of SWCNT-fibrinogen solution on a microscope slide, the clotting process was driven solely by diffusion, allowing us to follow the time-varying diffusion behavior of the SWCNTs incorporated within the clots. In contrast to the big clots that were formed under flow, we could not see large fibrin clusters in the quiescent droplet. Figure 9b shows a fluorescence image of the DPPE-PEG-SWCNTs with fibrinogen before the addition of thrombin and the displacement of three particles in the xy plane over several frames. The diffusion coefficient, calculated from the mean square displacement, for these particles was $(8.9 \pm 7.8)\ \mu m^2\ s^{-1}$. After the addition of thrombin, the SWCNTs diffusion slowed down significantly, as shown in Figure 9c for the three selected particles, for which the diffusion coefficient was only $(2.4 \times 10^{-4} \pm 8.1 \times 10^{-5})\ \mu m^2\ s^{-1}$. We attribute these changes in the diffusion coefficients to the formation of clots around the SWCNTs, which slows down the diffusion.

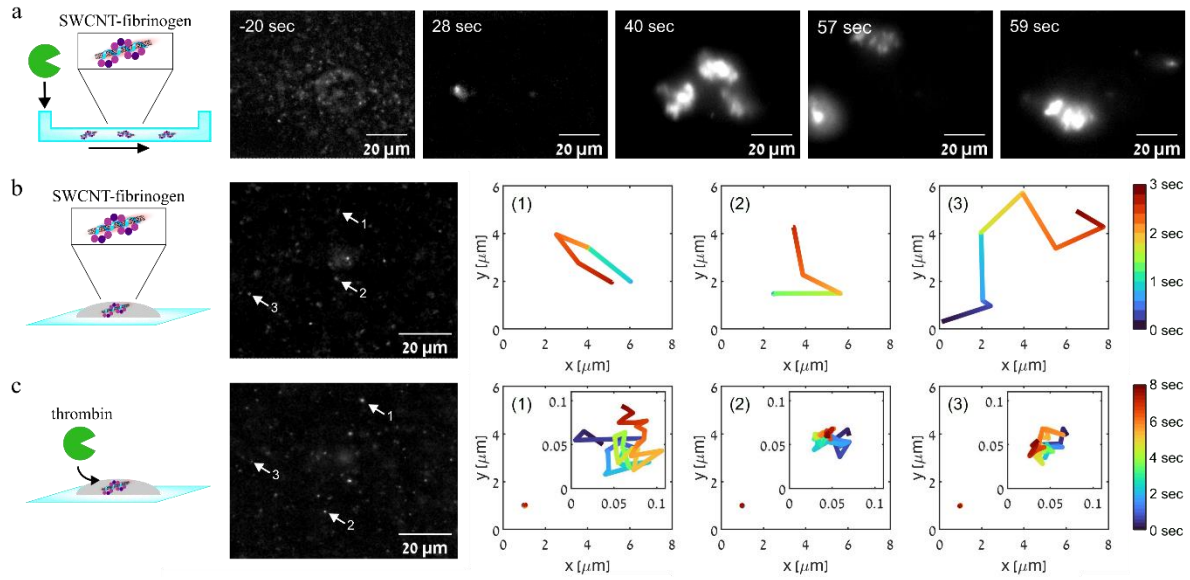

Figure 9. Time-resolved NIR-fluorescence imaging of DPPE-PEG-SWCNT–fibrinogen clotting process upon the addition of thrombin. a) Experiments performed in a µ-slide channel. Thrombin was added at t = 0 s. b) Experiments performed on a microscope slide. The temporal displacement of three individual DPPE-PEG-SWCNTs (marked with arrows) is displayed. c) Time-resolved NIR-fluorescence imaging of DPPE-PEG-SWCNT–fibrinogen after the addition of thrombin measured on a microscope slide. The temporal displacement of three single DPPE-PEG-SWCNTs (marked with arrows) is displayed. Inset: the same displacements over time at a large scale.

Owing to the significant change in the diffusion properties of the SWCNT before and after the addition of thrombin, the NIR fluorescence can be used to monitor the fibrin clotting with both spatial and temporal resolution. We, therefore, monitored the DPPE-PEG-SWCNT dynamics, aiming to detect changes in their diffusion when incorporated into the fibrin clots, with different concentrations of fibrinogen and thrombin. A SWCNT-fibrinogen solution was deposited on a microscope slide and the NIR fluorescence of the SWCNT was imaged continuously during and after the addition of thrombin in PBS and in 10% FBS. We tracked the trajectories of individual DPPE-PEG-SWCNTs during the clotting process and calculated the cumulative displacement of the particles over time. The cumulative displacement was compared for SWCNTs in different initial fibrinogen concentrations (Figure 10a, c) and for SWCNTs in solution with the same fibrinogen concentration upon the addition of thrombin at different concentrations (Figure 10b, d), in both PBS (Figure 10a, b) and serum (Figure 10c, d) environment. In all the experiments, we observed the same increase in the cumulative displacement before the addition of thrombin, indicating that the diffusion of the DPPE-PEG-SWCNTs did not depend on the fibrinogen concentration in the solution. After the addition of thrombin, the cumulative displacement of the DPPE-PEG-SWCNTs still increased, but with a rate that depended

on the fibrinogen concentration (Figure 10c) or the thrombin concentration (Figure 10d). A higher concentration of fibrinogen or thrombin resulted in a faster coagulation process, which was manifested in a faster decrease in the cumulative displacement rate. The concentration-dependent cumulative displacement curves can be used to formulate a calibration such that the concentration of fibrinogen or thrombin could be inferred from measured data based on a library of such curves for known concentrations. In addition, it can be used to test the final steps of the coagulation cascade where more upstream coagulation factors are tested. Therefore, these results open new possibilities to determine the concentration of clottable fibrinogen and active thrombin, and to develop new methods to monitor the coagulation cascade with real-time dynamic information, even in a complex environment.

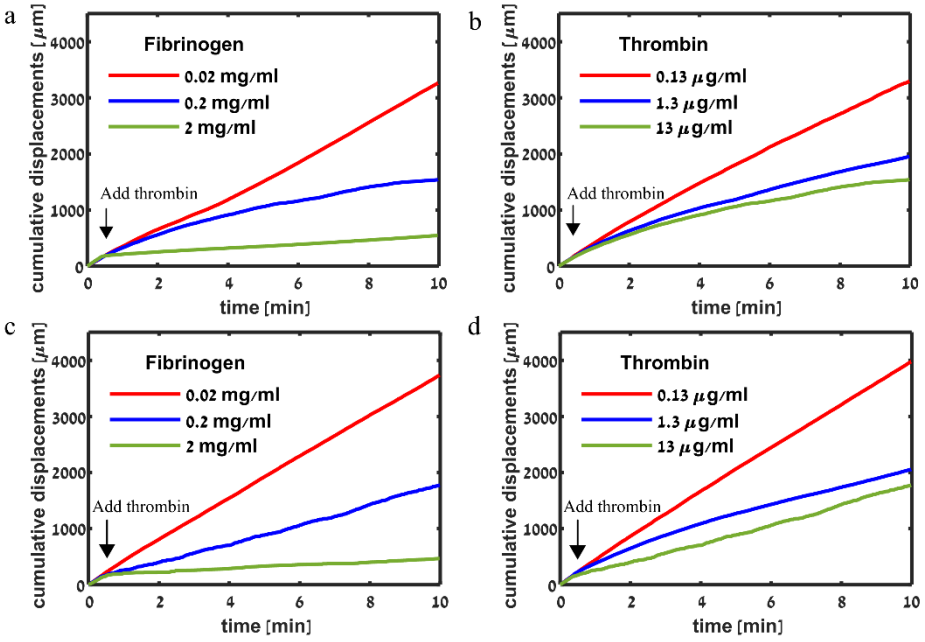

Figure 10. Time-resolved NIR-fluorescence imaging of DPPE-PEG-SWCNT-fibrinogen clotting process upon the addition of thrombin in PBS and in 10% FBS. a) Cumulative displacement over time of DPPE-PEG-SWCNT in PBS incubated with different concentrations of fibrinogen: 0.02 mg mL^{-1} (red), 0.2 mg mL^{-1} (blue), or 2 mg mL^{-1} (green) before and after the addition of 13 µg mL^{-1} thrombin. b) Cumulative displacement over time of DPPE-PEG-SWCNT in PBS incubated with 0.2 mg mL^{-1} fibrinogen before and after the addition of thrombin at different concentrations: 0.13 µg mL^{-1} thrombin (red), 1.3 µg mL^{-1} thrombin (blue), or 13 µg mL^{-1} thrombin (green) .c) Cumulative displacement over time of DPPE-PEG-SWCNT in 10% FBS incubated with different concentrations of fibrinogen: 0.02 mg mL^{-1} (red), 0.2 mg mL^{-1} (blue), or 2 mg mL^{-1} (green) before and after the addition of 13 µg mL^{-1} thrombin. d) Cumulative displacement over time of DPPE-PEG-SWCNT in 10% FBS incubated with 0.2 mg mL^{-1} fibrinogen before and after the addition of thrombin at different concentrations: 0.13 µg mL^{-1} thrombin (red), 1.3 µg mL^{-1} thrombin (blue), or 13 µg mL^{-1} thrombin (green).

5. Conclusion

We used the SWCNT fibrinogen sensor to monitor the formation of fibrin clots as part of the coagulation cascade. We found that the addition of thrombin did not affect the fluorescence emission of the SWCNTs, nor the peak absorption wavelengths, suggesting that fibrinogen remained bound to the SWCNT surface even after the addition of thrombin and that SWCNTs did not hinder clot formation. The incorporation of SWCNTs within the fibrin clots was evident from the darker color of a macroscale clot, visible to the naked eye. We further used NIR-fluorescence imaging to visualize the SWCNTs incorporated within the fibrin clots and found that the SWCNTs were indeed integrated into the fibrillary structures of the polymerized fibrin, in both buffer and serum. Moreover, compared to the low contrast of clots in bright-field imaging in the visible range, the SWCNTs fluorescence could be used as NIR staining of the clots, for precise localization and characterization. We succeeded in monitoring the dynamics of the clotting process in two different configurations, namely in a microfluidic channel under flow, and within a droplet on a microscope slide where the process is driven by diffusion alone. In the latter case, single particle tracking of individual SWCNTs in buffer or serum revealed different rates of clot formation depending on the concentrations of fibrinogen and thrombin, which could be used for the quantification of the clottable fibrinogen and active thrombin. These results suggest that SWCNTs are a promising platform for monitoring the formation of fibrin clots and for visualizing, localizing, and tracking fibrin clots in the NIR range with both spatial and temporal resolution. Building a library of the concentration-dependent cumulative displacement curves for known concentrations with more upstream coagulation factors will be the subject of a future study. Our method has the potential to improve our understanding of the blood coagulation process and could

advance the development of novel diagnostic and therapeutic strategies for coagulation disorders.

References

[1] B. Dahlbäck, *Lancet* **2000**, *355*, 1627.

[2] L. A. Norris, *Best Pract. Res. Clin. Obstet. Gynaecol.* **2003**, *17*, 369.

[3] D. Gailani, T. Renné, *Arterioscler. Thromb. Vasc. Biol.* **2007**, *27*, 2507.

[4] C. B. IJsselmuiden, R. R. Faden, *N. Engl. J. Med.* **1992**, *326*, 800.

[5] G. Bisker, J. Dong, H. D. Park, N. M. Iverson, J. Ahn, J. T. Nelson, M. P. Landry, S. Kruss, M. S. Strano, *Nat. Commun.* **2016**, *7*, 1.

[6] S. Herrick, O. Blanc-Brude, A. Gray, G. Laurent, *Int. J. Biochem. Cell Biol.* **1999**, *31*, 741.

[7] G. Guadiz, L. A. Sporn, R. A. Goss, S. O. Lawrence, V. J. Marder, P. J. Simpson-Haidaris, *Am. J. Respir. Cell Mol. Biol.* **1997**, *17*, 60.

[8] A. H. Henschen, *J. Protein Chem.* **1994**, *13*, 504.

[9] S. R. Coughlin, *Nature* **2000**, *407*, 258.

[10] J. P. Riddel, B. E. Aouizerat, C. Miaskowski, D. P. Lillicrap, *J. Pediatr. Oncol. Nurs.* **2007**, *24*, 123.

[11] K. E. Brummel, S. G. Paradis, S. Butenas, K. G. Mann, *Blood* **2002**, *100*, 148.

[12] K. G. Mann, S. Butenas, K. Brummel, *Arterioscler. Thromb. Vasc. Biol.* **2003**, *23*, 17.

[13] E. Di Cera, *Mol. Aspects Med.* **2008**, *29*, 203.

[14] E. W. Davie, J. D. Kulman, *Semin. Thromb. Hemost.* **2006**, *32*, 3.

[15] S. Kumar, S. Krishnaswamy, *Trauma Induc. Coagulopathy* **2016**, *124*, 55.

[16] D. A. Lane, H. Philippou, J. A. Huntington, *Blood* **2005**, *106*, 2605.

[17] K. Dammann, A. Gifford, K. Kelley, S. P. Stawicki, *Contemp. Appl. Biol. Hemostatic Agents across Surg. Spec.* **2020**, *2*, DOI 10.5772/intechopen.94100.

[18] K. E. Brummel-Ziedins, R. L. Pouliot, K. G. Mann, *J. Thromb. Haemost.* **2004**, *2*, 281.

[19] D. P. Hart, P. L. F. Giangrande, *Mol. Hematol.* **1991**, 89.

[20] K. M. Cawthern, C. Van't Veer, J. B. Lock, M. E. DiLorenzo, R. F. Branda, K. G. Mann, *Blood* **1998**, *91*, 4581.

[21] S. Butenas, K. E. Brummel, R. F. Branda, S. G. Paradis, K. G. Mann, *Blood* **2002**, *99*, 923.

[22] K. E. Brummel-Ziedins, C. Y. Vossen, S. Butenas, K. G. Mann, F. R. Rosendaal, *J. Thromb. Haemost.* **2005**, *3*, 2497.

[23] B. Furie, B. C. Furie, *J. Clin. Invest.* **2005**, *115*, 3355.

[24] F. R. Rosendaal, *Can. Conf. Electr. Comput. Eng.* **2001**, *2*, 725.

[25] P. De Moerloose, F. Boehlen, M. Neerman-Arbez, *Semin. Thromb. Hemost.* **2010**, *36*, 7.

[26] B. Sørensen, M. Tang, O. H. Larsen, P. N. Laursen, C. Fenger-Eriksen, C. J. Rea, *Thromb. Res.* **2011**, *128*, S13.

[27] K. G. Mann, K. Brummel-Ziedins, T. Orfeo, S. Butenas, *Blood Cells, Mol. Dis.* **2006**, *36*, 108.

[28] A. Tripodi, S. H. Caldwell, M. Hoffman, J. F. Trotter, A. J. Sanyal, *Aliment. Pharmacol. Ther.* **2007**, *26*, 141.

[29] A. H. Kamal, A. Tefferi, R. K. Pruthi, *Mayo Clin. Proc.* **2007**, *82*, 864.

[30] M. A. Khanin, D. V. Rakov, A. E. Kogan, *Thromb. Res.* **1998**, *89*, 227.

[31] A. L. Suchman, P. F. Griner, *Ann. Intern. Med.* **1986**, *104*, 810.

[32] E. J. Favaloro, G. Kershaw, S. Mohammed, G. Lippi, *Semin. Thromb. Hemost.* **2019**, *45*, 22.

[33] Y. L. Chee, J. C. Crawford, H. G. Watson, M. Greaves, *Br. J. Haematol.* **2008**, *140*, 496.

[34] D. Whiting, J. A. Dinardo, *Am. J. Hematol.* **2014**, *89*, 228.

[35] P. He, L. Liu, W. Qiao, S. Zhang, *Chem. Commun.* **2014**, *50*, 1481.

[36] T. T. Nguyen, S. O. Bea, D. M. Kim, W. J. Yoon, J.-W. Park, S. S. A An, H. Ju, *Int. J. Nanomedicine* **2015**, *10*, 155.

[37] S. Jo, I. Kim, W. Lee, M. Kim, J. Park, G. Lee, D. S. Yoon, J. Park, *Biosens. Bioelectron.* **2019**, *135*, 216.

[38] S. Li, D. Zhang, Q. Zhang, Y. Lu, N. Li, Q. Chen, Q. Liu, *Sensors Actuators, B Chem.* **2016**, *232*, 219.

[39] H. Aizawa, S. Kurosawa, M. Tozuka, J. W. Park, K. Kobayashi, *Sensors Actuators, B Chem.* **2004**, *101*, 150.

[40] Y. Wang, L. Bao, Z. Liu, D. W. Pang, *Anal. Chem.* **2011**, *83*, 8130.

[41] W. Wang, C. Chen, M. Qian, X. S. Zhao, *Anal. Biochem.* **2008**, *373*, 213.

[42] S. Niu, L. Qu, Q. Zhang, J. Lin, *Anal. Biochem.* **2012**, *421*, 362.

[43] M. V. Yigit, D. Mazumdar, Y. Lu, *Bioconjug. Chem.* **2008**, *19*, 412.

[44] L. Kuang, S. P. Cao, L. Zhang, Q. H. Li, Z. C. Liu, R. P. Liang, J. D. Qiu, *Biosens. Bioelectron.* **2016**, *85*, 798.

[45] H. Wei, B. Li, J. Li, E. Wang, S. Dong, *Chem. Commun.* **2007**, 3735.

[46] S. Centi, S. Tombelli, M. Minunni, M. Mascini, *Anal. Chem.* **2007**, *79*, 1466.

[47] Z. Lin, L. Chen, X. Zhu, B. Qiu, G. Chen, *Chem. Commun.* **2010**, *46*, 5563.

[48] J. Park, W. Lee, I. Kim, M. Kim, S. Jo, W. Kim, H. Park, G. Lee, W. Choi, D. S. Yoon, et al., *Sensors Actuators, B Chem.* **2019**, *293*, 296.

[49] M. Mohammadi Aria, A. Erten, O. Yalcin, *Front. Bioeng. Biotechnol.* **2019**, *7*, 1.

[50] L. G. Puckett, G. Barrett, D. Kouzoudis, C. Grimes, L. G. Bachas, *Biosens. Bioelectron.* **2003**, *18*, 675.

[51] E. Gerstman, A. Hendler-neumark, V. Wulf, G. Bisker, *ACS Appl. Mater. Interfaces* **2023**, *15*, 21866.

[52] P. M. Ajayan, J. C. Charlier, A. G. Rinzler, *Proc. Natl. Acad. Sci. U. S. A.* **1999**, *96*,

14199.

[53] S. M. Bachilo, M. S. Strano, C. Kittrell, R. H. Hauge, R. E. Smalley, R. B. Weisman, *Science (80-.).* **2002**, *298*, 2361.

[54] S. Kruss, A. J. Hilmer, J. Zhang, N. F. Reuel, B. Mu, M. S. Strano, *Adv. Drug Deliv. Rev.* **2013**, *65*, 1933.

[55] H. Amara, C. Bichara, *Top. Curr. Chem.* **2017**, *375*, 1.

[56] M. J. O'Connell, S. H. Bachilo, C. B. Huffman, V. C. Moore, M. S. Strano, E. H. Haroz, K. L. Rialon, P. J. Boul, W. H. Noon, C. Kittrell, et al., *Science (80-.).* **2002**, *297*, 593.

[57] J. Ackermann, J. T. Metternich, S. Herbertz, S. Kruss, *Angew. Chemie - Int. Ed.* **2022**, *61*, 1.

[58] A. Hendler-Neumark, G. Bisker, *Sensors (Switzerland)* **2019**, *19*, 1.

[59] M. P. Landry, L. Vuković,Vuković, S. Kruss, G. Bisker, A. M. Landry, S. Islam, R. Jain, K. Schulten, M. S. Strano, L. Vuković, et al., *J. Phys. Chem. C* **2015**, *119*, 10048.

[60] S. Wray, M. Cope, D. T. Delpy, J. S. Wyatt, E. O. R. Reynolds, *BBA - Bioenerg.* **1988**, *933*, 184.

[61] A. Hendler-Neumark, V. Wulf, G. Bisker, *Mater. Today Bio* **2021**, *12*, 1.

[62] R. Ehrlich, V. Wulf, A. Hendler-Neumark, B. Kagan, G. Bisker, *Opt. Express* **2022**, *30*, 1130.

[63] S. Kruss, M. P. Landry, E. Vander Ende, B. M. A. Lima, N. F. Reuel, J. Zhang, J. Nelson, B. Mu, A. Hilmer, M. Strano, *J. Am. Chem. Soc.* **2014**, *136*, 713.

[64] C. Bulumulla, A. T. Krasley, B. Cristofori-Armstrong, W. C. Valinsky, D. Walpita, D. Ackerman, D. E. Clapham, A. G. Beyene, *Elife* **2022**, *11*, 1.

[65] S. J. Yang, J. T. Del Bonis-O'Donnell, A. G. Beyene, M. P. Landry, *Nat. Protoc.* **2021**, *16*, 3026.

[66] P. W. Barone, R. S. Parker, M. S. Strano, *Anal. Chem.* **2005**, *77*, 7556.

[67] T. V. Galassi, M. Antman-Passig, Z. Yaari, J. Jessurun, R. E. Schwartz, D. A. Heller, *PLoS One* **2020**, *15*, 1.

[68] J. D. Harvey, P. V. Jena, H. A. Baker, G. H. Zerze, R. M. Williams, T. V. Galassi, D. Roxbury, J. Mittal, D. A. Heller, *Nat. Biomed. Eng.* **2017**, *1*, 1.

[69] B. Kagan, A. Hendler-Neumark, V. Wulf, D. Kamber, R. Ehrlich, G. Bisker, *Adv. Photonics Res.* **2022**, *3*, 1.

[70] N. M. Iverson, P. W. Barone, M. Shandell, L. J. Trudel, S. Sen, F. Sen, V. Ivanov, E. Atolia, E. Farias, T. P. McNicholas, et al., *Nat. Nanotechnol.* **2013**, *8*, 873.

[71] N. M. Iverson, G. Bisker, E. Farias, V. Ivanov, J. Ahn, G. N. Wogan, M. S. Strano, *J. Biomed. Nanotechnol.* **2016**, *12*, 1035.

[72] M. Son, P. Mehra, F. T. Nguyen, X. Jin, V. B. Koman, X. Gong, M. A. Lee, N. A. Bakh, M. S. Strano, *ACS Nano* **2022**, 1.

[73] M. A. Lee, S. Wang, X. Jin, N. A. Bakh, F. T. Nguyen, J. Dong, K. S. Silmore, X. Gong, C. Pham, K. K. Jones, et al., *Adv. Healthc. Mater.* **2020**, *9*, 1.

[74] V. B. Koman, N. A. Bakh, X. Jin, F. T. Nguyen, M. Son, D. Kozawa, M. A. Lee, G. Bisker, J. Dong, M. S. Strano, *Nat. Nanotechnol.* **2022**, *17*, 643.

[75] A. Jain, A. Homayoun, C. W. Bannister, K. Yum, *Biotechnol. J.* **2015**, *10*, 447.

[76] F. A. Mann, Z. Lv, J. Großhans, F. Opazo, S. Kruss, *Angew. Chemie - Int. Ed.* **2019**, *58*, 11469.

[77] K. Welsher, S. P. Sherlock, H. Dai, *Proc. Natl. Acad. Sci. U. S. A.* **2011**, *108*, 8943.

[78] A. G. Godin, J. A. Varela, Z. Gao, N. Danné, J. P. Dupuis, B. Lounis, L. Groc, L. Cognet, *Nat. Nanotechnol.* **2017**, *12*, 238.

[79] A. G. Beyene, K. Delevich, J. T. Del Bonis-O'Donnell, D. J. Piekarski, W. C. Lin, A. Wren Thomas, S. J. Yang, P. Kosillo, D. Yang, G. S. Prounis, et al., *Sci. Adv.* **2019**, *5*, 1.

[80] E. M. Hofferber, J. A. Stapleton, N. M. Iverson, *J. Electrochem. Soc.* **2020**, *167*, 1.

[81] E. Hofferber, J. Meier, N. Herrera, J. Stapleton, C. Calkins, N. Iverson, *Nanomedicine Nanotechnology, Biol. Med.* **2022**, *40*, 1.

[82] V. C. Moore, M. S. Strano, E. H. Haroz, R. H. Hauge, R. E. Smalley, J. Schmidt, Y. Talmon, *Nano Lett.* **2003**, *3*, 1379.

[83] A. A. Boghossian, J. Zhang, P. W. Barone, N. F. Reuel, J. H. Kim, D. A. Heller, J. H. Ahn, A. J. Hilmer, A. Rwei, J. R. Arkalgud, et al., *ChemSusChem* **2011**, *4*, 848.

[84] P. V. Jena, M. M. Safaee, D. A. Heller, D. Roxbury, *ACS Appl. Mater. Interfaces* **2017**, *9*, 21397.

[85] J. Meier, J. Stapleton, E. Hofferber, A. Haworth, S. Kachman, N. M. Iverson, *Nanomaterials* **2021**, *11*, 1.

[86] M. Gravely, A. Kindopp, L. Hubert, M. Card, A. Nadeem, C. Miller, D. Roxbury, *ACS Appl. Mater. Interfaces* **2022**, *14*, 19168.

[87] H. Wu, R. Nißler, V. Morris, N. Herrmann, P. Hu, S. J. Jeon, S. Kruss, J. P. Giraldo, *Nano Lett.* **2020**, *20*, 2432.

[88] H. Wang, A. A. Boghossian, *Mater. Adv.* **2022**, *1*, 525.

[89] D. A. Heller, G. W. Pratt, J. Zhang, N. Nair, A. J. Hansborough, A. A. Boghossian, N. F. Reuel, P. W. Barone, M. S. Strano, *Proc. Natl. Acad. Sci. U. S. A.* **2011**, *108*, 8544.

[90] M. M. Alvarez, J. Aizenberg, M. Analoui, A. M. Andrews, G. Bisker, E. S. Boyden, R. D. Kamm, J. M. Karp, D. J. Mooney, R. Oklu, et al., *ACS Nano* **2017**, *11*, 5195.

[91] G. Bisker, J. Ahn, S. Kruss, Z. W. Ulissi, D. P. Salem, M. S. Strano, *J. Phys. Chem. C* **2015**, *119*, 13876.

[92] B. Lambert, A. J. Gillen, N. Schuergers, S. J. Wu, A. A. Boghossian, *Chem. Commun.* **2019**, *55*, 3239.

[93] Z. Yaari, Y. Yang, E. Apfelbaum, C. Cupo, A. H. Settle, Q. Cullen, W. Cai, K. L. Roche, D. A. Levine, M. Fleisher, et al., *Sci. Adv.* **2021**, *7*, 1.

[94] V. Wulf, G. Bisker, *Nano Lett.* **2022**, *22*, 9205.

[95] V. Wulf, E. Bichachi, A. Hendler-Neumark, T. Massarano, A. B. Leshem, A. Lampel, G. Bisker, *Adv. Funct. Mater.* **2022**, *2209688*, 1.

[96] V. Shumeiko, Y. Paltiel, G. Bisker, Z. Hayouka, O. Shoseyov, *Biosens. Bioelectron.* **2021**, *172*, 1.

[97] V. Shumeiko, E. Malach, Y. Helman, Y. Paltiel, G. Bisker, Z. Hayouka, O. Shoseyov, *Sensors Actuators B. Chem.* **2021**, *327*, 1.

[98] M. Dinarvand, S. Elizarova, J. Daniel, S. Kruss, *Chempluschem* **2020**, *85*, 1465.

[99] P. V. Jena, D. Roxbury, T. V. Galassi, L. Akkari, C. P. Horoszko, D. B. Iaea, J. Budhathoki-Uprety, N. Pipalia, A. S. Haka, J. D. Harvey, et al., *ACS Nano* **2017**, *11*, 10689.

[100] J. Zhang, M. P. Landry, P. W. Barone, J. H. Kim, S. Lin, Z. W. Ulissi, D. Lin, B. Mu, A. A. Boghossian, A. J. Hilmer, et al., *Nat. Nanotechnol.* **2013**, *8*, 959.

[101] D. Amir, A. Hendler-Neumark, V. Wulf, R. Ehrlich, G. Bisker, *Adv. Mater. Interfaces* **2022**, *9*, 1.

[102] V. Shumeiko, Y. Zaken, G. Hidas, Y. Paltiel, G. Bisker, O. Shoseyov, *IEEE Sens. J.* **2022**, *22*, 6277.

[103] G. Bisker, N. A. Bakh, M. A. Lee, J. Ahn, M. Park, E. B. O'Connell, N. M. Iverson, M. S. Strano, *ACS Sensors* **2018**, *3*, 367.

[104] R. Ehrlich, A. Hendler-Neumark, V. Wulf, D. Amir, G. Bisker, *Small* **2021**, *17*, 1.

[105] R. L. Pinals, F. Ledesma, D. Yang, N. Navarro, S. Jeong, J. E. Pak, L. Kuo, Y. C. Chuang, Y. W. Cheng, H. Y. Sun, et al., *Nano Lett.* **2021**, *21*, 2272.

[106] S. Y. Cho, X. Jin, X. Gong, S. Yang, J. Cui, M. S. Strano, *Anal. Chem.* **2021**, *93*, 14685.

[107] R. M. Williams, J. D. Harvey, J. Budhathoki-Uprety, D. A. Heller, *Nano Lett.* **2020**, *20*, 7287.

[108] Z. Yaari, J. M. Cheung, H. A. Baker, R. S. Frederiksen, P. V. Jena, C. P. Horoszko, F. Jiao, S. Scheuring, M. Luo, D. A. Heller, *Nano Lett.* **2020**, *20*, 7819.

[109] V. Shumeiko, Y. Paltiel, G. Bisker, Z. Hayouka, O. Shoseyov, *Sensors (Switzerland)* **2020**, *20*, 1.

[110] V. Wulf, G. Slor, P. Rathee, R. J. Amir, G. Bisker, *ACS Nano* **2021**, *15*, 20539.

[111] D. Loewenthal, D. Kamber, G. Bisker, *Anal. Chem.* **2022**, *94*, 14223.

[112] J. Y. Tinevez, N. Perry, J. Schindelin, G. M. Hoopes, G. D. Reynolds, E. Laplantine, S. Y. Bednarek, S. L. Shorte, K. W. Eliceiri, *Methods* **2017**, *115*, 80.

[113] N. A. Barinov, E. R. Pavlova, A. P. Tolstova, A. G. Matveeva, A. P. Moskalets, E. V. Dubrovin, D. V. Klinov, *Microsc. Res. Tech.* **2022**, *85*, 2537.

תקציר

קרישת דם היא מנגנון הגנה קריטי מפני דימום הגורמת להמרת דם נוזלי לקריש מוצק באמצעות מפל ריאקציות מסובך, הכולל מספר גורמי קרישה. אחד השלבים האחרונים במסלול הקרישה הוא הפיכת פיברינוגן לפיברין בלתי מסיס בתיווך תרומבין. מכיוון שהפרעות קרישה עלולות להיות מסכנות חיים, יש חשיבות גבוהה לפיתוח שיטות חדשות לניטור דינמי של מפל הקרישה.

כאן, אנו משתמשים בננו-צינוריות פחמן חד-שכבתיות (SWCNT) הפולטות פלורסנציה באינפרא-אדום הקרוב (NIR) לצילום ולניטור קרישת פיברין, בזמן אמת. SWCNTs ניתנים לתיאור כיריעות גרפין המגולגלות לגלילים ארוכים וחלולים הפולטים פלורסנציה באזור הספקטרלי האינפרא-אדום הקרוב. ל- SWCNTs יתרונות רבים כחיישני פלורסנציה עבור יישומים ביו-רפואיים, בעיקר בזכות התאימות הביולוגית שלהם, והפליטה הפלורסנטית בחלון הביולוגי השקוף. לאחר קישור של פיברינוגן לפלטפורמת SWCNT מותאמת, תרומבין הופך את הפיברינוגן למונומרים של פיברין, שמתחילים להתפלמר. ה-SWCNTs משולבים בתוך הקריש וניתן לחזות בהם בבירור בערוץ האינפרא אדום הקרוב, שבו יחס האות לרעש משופר בהשוואה לדימות בטווח הנראה. יתרה מכך, הדיפוזיה של SWCNTs בודדים בתוך קריש הפיברין מואטת בהדרגה לאחר הוספת תרומבין, המתבטאת בקצב קרישה שתלוי הן בריכוז הפיברינוגן והן בריכוז התרומבין. הפלטפורמה שלנו יכולה לפתוח הזדמנויות חדשות לאבחון הפרעות קרישה ולאפשר ניטור בזמן אמת של מפל הקרישה עם פלט אות אופטי בטווח האינפרא אדום הקרוב בזמן אמת, בחלון השקיפות הביולוגית.

אוניברסיטת תל - אביב

הפקולטה להנדסה ע"ש איבי ואלדר פליישמן

בית הספר לתארים מתקדמים ע"ש זנדמן-סליינר

שימוש בננו-ציניריות פחמן חד-שכבתיות הפולטות פלורסנציה לניטור היווצרות קרישי פיברין כחלק ממפל הקרישה

חיבור זה הוגש כעבודת גמר לקראת התואר "מוסמך אוניברסיטה" בהנדסה ביו-רפואית

על-ידי

אפרת גרסטמן

העבודה נעשתה במחלקה להנדסה ביו-רפואית

בהנחית ד"ר גילי ביסקר

סיון תשפ"ג

אוניברסיטת תל - אביב

הפקולטה להנדסה ע"ש איבי ואלדר פליישמן

בית הספר לתארים מתקדמים ע"ש זנדמן-סליינר

שימוש בננו-ציניריות פחמן חד-שכבתיות הפולטות פלורסנציה לניטור היווצרות קרישי פיברין כחלק ממפל הקרישה

חיבור זה הוגש כעבודת גמר לקראת התואר "מוסמך אוניברסיטה" בהנדסה ביו-רפואית

על-ידי

אפרת גרסטמן

סיון תשפ"ג